Advancing Local Distance Discrimination of Explosions and Earthquakes with Joint P/S and ML-MC Classification

Ruijia Wang[1], Brandon Schmandt[1], Monique Holt[2], and Keith D. Koper[2]

[1]University of New Mexico
[2]University of Utah

November 22, 2022

Abstract

Classification of local-distance, low-magnitude seismic events is challenging because signals can be numerous and difficult to characterize with approaches developed for larger magnitude events observed at greater distances. Yet, accurate classification is important to studies of earthquake processes and detection of potential underground nuclear tests. Here, we combine two classification metrics: the three-component ratio of high-frequency P/S amplitudes and the difference between local and coda duration magnitudes (M_L-M_C). The metrics use different parts of the high-frequency wavefield and exhibit complementary sensitivity for classification of M˜0.5–4 natural earthquakes and borehole explosions, which are the best analog for underground nuclear explosions. Using means from bootstrap resampling across four diverse geologic settings, joint classification achieves >94.4% true positives and <8.4% false positives when using >=8 seismographs within 200 km. This high performance is obtained without local site corrections, indicating that the method may be transportable for local event classification.

Hosted file

`essoar.10507788.1.docx` available at https://authorea.com/users/528476/articles/598889-advancing-local-distance-discrimination-of-explosions-and-earthquakes-with-joint-p-s-and-ml-mc-classification

Advancing Local Distance Discrimination of Explosions and Earthquakes with Joint P/S and M_L-M_C Classification

Ruijia Wang[1,2], Brandon Schmandt[1], Monique Holt[3,4], and Keith Koper[3]

1. Department of Earth and Planetary Sciences, University of New Mexico, Albuquerque, NM, US

2. Department of Earth and Space Sciences, Southern University of Science and Technology, Shenzhen, Guangdong, China

3. Department of Geology and Geophysics, University of Utah, Salt Lake City, Utah, US

4. Department of Earth and Environmental Sciences, University of Illinois at Chicago, Chicago, Illinois, US

Corresponding author: `ruijia.wang@ualberta.ca`

Key points:

1. P/S ratio and M_L-M_C exhibit complementary sensitivity for discriminating earthquakes and single-fired explosions.
2. Excellent classification performance is achieved in four diverse tectonic settings without local site corrections.
3. The new methodology will improve the ability to identify low-yield underground explosions.

Key words:

Local-regional earthquakes; Explosive sources; Seismic source classification; U.S continent; Body wave ratios; Local and coda magnitudes

Abstract

Classification of local-distance, low-magnitude seismic events is challenging because signals can be numerous and difficult to characterize with approaches developed for larger magnitude events observed at greater distances. Yet, accurate classification is important to studies of earthquake processes and detection of potential underground nuclear tests. Here, we combine two classification metrics: the three-component ratio of high-frequency P/S amplitudes and the difference between local and coda duration magnitudes (M_L-M_C). The metrics use different parts of the high-frequency wavefield and exhibit complementary sensitivity for classification of **M**~0.5–4 natural earthquakes and borehole explosions, which are the best analog for underground nuclear explosions. Using means from bootstrap resampling across four diverse geologic settings, joint classification achieves >94.4% true positives and <8.4% false positives when using >=8 seismographs within 200 km. This high performance is obtained without local site corrections, indicating that the method may be transportable for local event classification.

Plain-Language Summary

Separating explosive sources from earthquakes is fundamental to seismic monitoring and seismic hazard evaluation. Many methods have been developed to discriminate between the two types of events, mostly taking advantage of depth differences and/or the energy ratios between seismic phases. However, these methods may be less effective at local scales (i.e., <200 km) and discrimination parameters often need to be calibrated to adapt to various regional settings. In this study, we collected hundreds of **M**~0.5–4 earthquakes and borehole explosions from four regions in the western U.S. and tested two popular discrimination methods: 1) body-wave energy ratio (P/S) and 2) magnitude differences (M_L-M_C). We find the two metrics complement each other, providing better discrimination in all four regions with station numbers as low as ~8. Furthermore, the joint method shows less dependence on local crustal setting, thus, it may be applicable to new regions with complex geological settings or scarce calibration data.

1 Introduction

Accurate classification of explosive seismic sources and earthquakes is a key component for agencies monitoring compliance with nuclear test ban treaties (e.g., Bowers & Selby, 2009) and for hazard mitigation agencies monitoring earthquake activity (e.g., Renouard *et al.*, 2021). Seismic discrimination of underground explosions has been successful for larger magnitude events that are typically observed at teleseismic distances (i.e., >3,000 km), however discrimination at local distances (< 200 km) remains challenging. Unidentified explosions can bias earthquake statistics and increase uncertainty of seismic hazard prediction (Mackey *et al.*, 2003; Astiz *et al.*, 2014; Gulia & Gasperini, 2021; Marzen *et al.*, 2021). Furthermore, mining blasts (Dokht *et al.*, 2020) and underground weapons tests (Tian *et al.*, 2018; Walter *et al.*, 2018) may temporarily increase regional seismic hazard via activation of local faults or collapse events (Walter *et al.*, 2018). Thus, discrimination of small explosions and earthquakes at local distances remains crucial. However, adaptation of teleseismic methods to local scales and smaller magnitudes is challenged by factors like weaker and higher-frequency seismic phases, highly variable geological structures, and limited station coverage (Taylor *et al.*, 1989; Hartse *et al.*, 1997; O'Rourke *et al.*, 2016).

Local-scale source classification, including machine-learning based techniques (e.g., Linville *et al.*, 2019), relies more on high frequency body wave measurements such as P/S ratios because long period surface waves are barely excited by small magnitude events (e.g., Taylor *et al.*, 1989; Kim *et al.*, 1993; O'Rourke & Baker, 2017; Walter *et al.*, 2018). Accordingly, depth-sensitive magnitude-based screening metrics, like the difference between local and coda duration magnitudes (M_L-M_C), have been proposed and successfully applied to several regions (Zeiler & Velasco, 2009; Holt *et al.*, 2019; Voyles *et al.*, 2020; Koper *et al.*, 2021), replacing the difference between teleseismic body wave and surface wave magnitudes (m_b:M_S) that is commonly used for larger events (Stevens & Day, 1985; Russell, 2006; Selby *et al.*, 2012). Although both methods mentioned above show potential for local-scale discrimination, empirical corrections from global-to-regional studies may be difficult to adapt to local crustal wave propagation (Walter *et al.*, 1995; Walter & Taylor, 2001; Anderson *et al.*, 2009). Such corrections and regional calibrations usually rely on high-resolution structure models and/or sufficient pre-classified events for learning (e.g., Fisk *et al.*, 1996; Rabin *et al.*, 2016). Furthermore, region-specific calibration requirements degrade the transportability of discrimination methods (Douglas, 2007).

The rapid growth of local-to-regional seismic data in recent years motivates revisiting classic waveform-based discrimination methods at local distances (O'Rourke *et al.*, 2016; Pyle & Walter, 2019; Wang *et al.*, 2020; Koper *et al.*, 2021). In this study, we systematically calculated P/S ratio and M_L-M_C values for earthquakes and borehole explosives recorded at distances $<$ 200 km by dozens of seismometers in four distinct regions. Uniform processing for four local-distance datasets enables more direct comparison than is possible among prior studies using variable processing workflows and distance ranges. Performance of our joint metric is evaluated by systematically decreasing station coverage for individual and merged datasets to simulate a variety of more realistic monitoring conditions. We show that accurate discrimination could be achieved with minimal local knowledge (i.e., an approximate 1-D velocity model) and the joint method is transportable across various local-regional settings.

2 Datasets

We aim to collect local seismic observations of single-fired explosive sources and earthquakes at comparable scales but variable tectonic settings. Toward this goal, four datasets in the U.S. are used (Figure 1): Mount St. Helens magma imaging project (MSH) in Washington, the Bighorn Arch Seismic Experiment (BASE) in Wyoming, the Source Physics Experiment 1 (SPE) in Nevada, and the Salton Seismic Imaging Project (SSIP) in California. As borehole shots are effective proxies for underground nuclear tests (Stump *et al.*, 2002), we focus on a binary discrimination between borehole shots and earthquakes (i.e., mine blasts from BASE are excluded). The four datasets contain 90 borehole shots and ~290 earthquakes with comparable magnitudes and event-station distances, which are concentrated at <200 km (Figure S1).

2.1 Mount St. Helens (MSH)

Nearly 90 broadband stations recorded 23 explosive sources (M_L 0.9–2.3) and 91 earthquakes (M_L 1.5–3.3, as reported by USGS) within 75 km of the volcano during the 2014–2016 iMUSH project (Figure 1a; Han *et al.*, 2016, Ulberg *et al.*, 2020). The explosive events are shallow borehole shots with explosive loads of either 454 or 907 kg, forming a relatively uniform distribution around the volcano. Earthquakes (depth<20 km) in this region are broadly distributed as well, with slightly more events located in the St. Helens seismic zone and West Rainier seismic zone (Figure 1a; Stanley *et al.*, 1996).

2.2 Bighorn Arch Seismic Experiment (BASE)

The BASE project was conducted in 2010 to image the Bighorn Arch (Figure 1b; Worthington *et al.*, 2016). The dataset contains 21 explosive sources (M_L 0.7–1.7; loads 113–907 kg), 19 earthquakes (M_L 0.3–2.7), and 37 mine blasts (M_L1.8–3.3) recorded by ~90 broadband stations and ~180 short-period stations. Most mine blasts are located to the southeast of the array with potential loads on the order of 10,000 kg (O'Rourke *et al.*, 2016). P/S ratio and M_L-M_C results for the mine blasts in BASE are shown in Figure 2 for readers' interest.

2.3 Source Physics Experiment Phase 1 (SPE)

Five borehole shots (M_L 1.2–2.1, loads 90–5,035 kg) are available for SPE Phase 1 in 2011, which occurred in the area of prior underground nuclear explosion tests in the U.S. (Figure 1c; Snelson *et al.*, 2013). They are fired at the same location at the center of the array with variable depths (see Figure 1c). The station coverage of these events ranges from ~3-35, which makes it the smallest among the four datasets. We used 110 earthquakes (M_L 1.0–4.4) that occurred in the area during or after 2011.

2.4 Salton Sea Imaging Project (SSIP)

SSIP conducted an active source seismic survey in 2011 to image crustal faults and constrain rifting processes (Figure 1d; Han *et al.*, 2016; Fuis *et al.*, 2017). Up to ~80 broadband stations were available during SSIP in 2011 and 126 explosions were single-fired with loads ranging from 3 to 1,440 kg. To ensure a comparable magnitude to earthquakes and the other 3 datasets, we only used 41 shots with loads >200 kg (M_L 0.6–2.1). The USGS catalog returns 76 events (M_L 1–3.6) during the month, including 6 borehole shots mis-cataloged as earthquakes (Table S1). The remaining earthquakes are mostly located within Mexico along the Imperial Fault Zone, potential aftershocks of the **M**7.2 Baja California earthquake (e.g., Castro *et al.*, 2011).

3 Methods

3.1 P/S ratio analysis

Four regional 1-D velocity models are used to predict the P or S phase arrivals of events at the corresponding datasets (Figure S2). All broadband or high gain three-component records are filtered between 10–18 Hz because that was found to be optimal for local-distance P/S discrimination by Wang *et al.* (2020). The P/S ratios are then calculated from the effective variance of given phases using Eq (1).

$$P/S = \frac{\sqrt{(P_R^2+P_T^2+P_Z^2)-(N_R^2+N_T^2+N_Z^2)}}{\sqrt{(S_R^2+S_T^2+S_Z^2)-(N_R^2+N_T^2+N_Z^2)}} \text{ , Eq (1)}$$

where, R, T, Z denotes the radial, transverse, and vertical component recordings for P-, S- and noise (N) windows, respectively. Three-component SNRs are also calculated using the same P windows and noise windows 10 sec before P arrival. A consistent cutoff of SNR>2 is required for a valid P/S ratio of the given event-station pair. Considering the distance ranges, no pre-S noise is involved, as the P-coda may continue until the S-wave arrival. Therefore, our SNR threshold purposely admits events with low S amplitudes. No site correction (e.g., MDAC, Walter & Taylor, 2001) is applied and the final event-based P/S ratio is determined from the median value of all stations with valid P/S ratio measurements. The final P/S ratios are calculated with only 1-D velocity models and earthquake/explosive catalogs as inputs. More details on parameters and comparison to methods from previous studies are provided in Text S2.

3.2 $\mathrm{M_L}$-$\mathrm{M_C}$

$\mathrm{M_L}$ and $\mathrm{M_C}$ values for all events are calculated from the waveforms; none of the $\mathrm{M_L}$ values are adopted from the USGS or local monitoring catalogs. Thus, all magnitude calculations are conducted without prior information of source type. To emulate the situation that might exist when testing begins in a new region, a consistent calibration of both $\mathrm{M_L}$ and $\mathrm{M_C}$ (optimized for Utah) is applied to all datasets (e.g., Koper *et al.*, 2021).

When calculating $\mathrm{M_L}$, the regional broadband seismic records (i.e., HH and BH components) are first converted to Wood-Anderson seismometer equivalent response. The station amplitude is then measured from the two horizontal-components without station corrections and distance corrections are applied (e.g., Richter, 1958).

For $\mathrm{M_C}$ calculation, the formula inherits the current duration magnitude definitions of UUSS (Pechmann *et al.*, 2006) with a modified cutoff threshold (SNR=2). All vertical components of high gain seismometers are corrected for instrument response and filtered between 1–10Hz. The seismogram envelopes are generated for coda windowing, which starts near the maximum S-wave amplitude and ends with the designated SNR cutoff. The M_C at a station is then calculated from the measured coda duration using the equations described in Koper *et al.* (2021). Note that the SNRs here are from single (vertical) components, different from the three-component SNR used for P/S ratio at higher frequencies (10–18 Hz). For both M_L and M_C measurements, the final event magnitudes are determined as the median from >3 valid station-based measurements.

3.3 Performance evaluation using ROC curve and Mahalanobis distance

The best threshold values for source type classification with either P/S ratio or M_L-M_C are obtained via grid searches to optimize the Area Under the Curve (AUC) defined by the Receiver Operating Characteristic (ROC). The ROC curve (Figure S5) jointly considers the true positive rate (TPR) and false positive rate (FPR) for binary classification (Fawcett, 2006). In our case, the explosions are defined as "positive", and earthquakes are defined as "negative". Such evaluation is event-based, where the median value of the P/S ratio or M_L-M_C from all valid stations (>3) is determined as the final value for that event. In the joint domain, the best cutoff line is also obtained by grid searching using a 2-D parameter space of slope and intercept to maximize the AUC (Figure S6).

When all the events are finalized with a combination of P/S ratio and M_L-M_C, the Mahalanobis distance (Δ^2) between two types of events is calculated using the mean and covariance values. The distances do not hold any specific physical meaning but are often used as a mathematical evaluation to define the "closeness" of two populations in a given parameter space (i.e., P/S ratio and M_L-M_C). We refer readers to the supporting materials and previous publications for details (e.g., Tibi, 2021). In general, AUC evaluates a discrimination that has been performed on known datasets, whereas Mahalanobis distances could reflect the robustness of the discriminations that may transfer to future applications.

4 Results

4.1 Individual metrics

Among the four different settings, the optimal P/S ratio and M_L-M_C cutoffs vary between 0.9–1.5 and -0.15–0.3, respectively (Figure 2). The best P/S ratio cutoffs are comparable between regions (~1) and highest for SPE. BASE requires the lowest individually optimized P/S ratio cutoff (0.9–1.1 achieve identical performance) but the highest M_L-M_C cutoff (0.3). For all four datasets, P/S ratios provide more robust discrimination than M_L-M_C based on TPR (recall) and FPR, which were used to optimize the discrimination threshold. Precision (i.e., true positives/total positives) is also given as an additional performance measure (Table 1). For MSH, BASE and SPE, optimal P/S ratio cutoffs could identify the explosions with only a few false alarms, whereas M_L-M_C results in higher FPR. The precision (0.6 and 0.23) is low for both metrics at SPE, as only three explosives meet our quality control (i.e., low station coverage). In addition, we did not observe apparent distance-dependence of P/S ratios from the four datasets at <200 km (Text S2 and Figure S3). As short period stations are used for P/S calculations, whereas M_L-M_C requires broadband stations, most events across the four datasets have a higher number of valid stations for P/S ratio than for M_L-M_C (Figure S5).

4.2 Joint method

A total of 68 explosives and 262 earthquakes were analyzed with a minimum magnitude of 0.6 and 0.7, respectively. The two groups are well-separated in the joint P/S and M_L-M_C domain (Figure 2). The best joint cutoffs are determined from grid-searching over slopes and intercepts (Figure S6) and the optimal values are reported in Table 1. For individual datasets, a wide range of slopes (~0.7–2.5) are acceptable except for SSIP (see Figure S6), suggesting a comparable contribution from both methods. The low slope value obtained for SSIP is likely affected by the single explosion with P/S ratio <1 (Figure 2d). Overall, the joint method achieves better performance for all four datasets (Table 1), leading to TPR=100% and FPR<1.2%. For regions that P/S ratio alone achieved TPR=100%, the joint method increases precision by ~15% (i.e., MSH and SPE) by rejecting more false positives.

Compared to earlier studies of local to regional seismic source discrimination (e.g., Bennett *et al.*,1986), the performance of our joint discrimination approach benefits from dense station coverage in the four study regions (see Figure 1). Thus, we tested the station-coverage effect via bootstrapping: a given number of stations are randomly selected (without repetition) and we require no SNR threshold. In other words, valid stations are often less than the total number of stations used within each trial to simulate the realistic circumstance in which not all stations have adequate SNR for a specific event. For each total number of stations, random selection is repeated 1,000 times and the mean (and standard deviation) of the TPR and FPR are recorded (Figure 3). As expected, the discrimination performance increases with station coverage and larger variations are observed when a dataset contains fewer events (e.g., SPE). Meanwhile, decent TPR (64.4%–94.5%) and FPR (5.8%–22.2%) could be achieved with 8 stations. Improvement is limited (<5%) with >32 stations.

5 Discussion

The joint method demonstrates promising transportability for uniformly processed datasets. Although the discrimination thresholds vary between regions—especially for M_L-M_C —the explosive sources and earthquakes always fall into two clusters in the P/S versus M_L-M_C domain. Surprisingly, such separation is preserved even after merging all four datasets: the covariance ellipses remain separated at 1 standard deviation (Figure 4a). Similarly high TPR (>95%) and low FPR (<5%) are achieved when a joint cutoff line is used rather than individually optimized cutoffs for each array, leading to a maximum AUC=0.9755 (Figure 4b). In fact, such discrimination performance can be achieved with fewer stations, for example, 8-stations leads to averaged TPR=94.4% and FPR=8.4% (Figure 4c) with <5% variations for both, comparable to the performance of supervised machine-learning (e.g., Reynen & Audet, 2017). In addition, our approach is particularly effective for identifying the true explosives, with only 1 out of 66 borehole shots resulting in a false negative classification.

The Mahalanobis distance (and minimum probability of mis-classification P_M; Text S4) between the two populations increases (decreases) to 18.5 (1.6%) in the joint domain, whereas P/S and M_L-M_C result in 15.4 (2.5%) and 2.6 (21.1%), respectively. Such improvement could be explained by three types of complementary sensitivities between P/S and M_L-M_C: frequency, depth, and distance. First, the two methods focus on different frequency ranges, with P/S ratios calculated at 10–18 Hz, M_C at 1–10 Hz and M_L at <1.25 Hz. Second, previous studies suggested that M_L-M_C screening is sensitive to event depth because shallow events create stronger coda (Holt *et al.*, 2019), while P/S ratio exhibits less sensitivity to depth at local distances (Wang *et al.*, 2020). Lastly, the depth-sensitivity of M_L-M_C is more effective at near-distances, evidenced by increased slope of the "combined" discrimination threshold line reflecting higher contribution from M_L-M_C (Figure 4d). In addition, when restricting the combined dataset to near distances, the relatively low Mahalanobis distances imply worse separation between the two populations (Figure 4d), echoing the reduced performance of P/S-ratio based discrimination near the source in some prior studies (e.g., O'Rourke *et al.*, 2016, Pyle & Walter, 2019). We speculate that such near-distance challenges may partly reflect poorer station coverage, which diminishes at distances at ~60 km for the four datasets (Figure S1). Regardless of the root factor that challenges near-source P/S-ratio-based discrimination, adding M_L-M_C measurements leads to a stable and high AUC (>0.95) across all distances.

The success of our joint discrimination is somewhat influenced by data selection, in which any events missing any of the three measurements (i.e., P/S ratio, M_L, and M_C) are excluded from the classification test. As a result, 23 earthquakes and 21 explosive events were not analyzed in the joint domain. However, we note that all explosions can still be discriminated by P/S ratio alone (i.e., P/S>1), albeit with a higher FPR (26%) than we found for the events included in the joint analysis (e.g., Figure S9, also see Table S1). Therefore, the high performance achieved by our joint discrimination is not strongly biased by the quality controls governing data selection.

Unlike previous locally specific discrimination studies that demand site (e.g., Wang *et al.*, 2021), path (e.g., Rodgers *et al.*, 1999) and/or magnitude corrections (e.g., Walter *et al.*, 1995), the joint method as implemented here does not rely on locally-specific pre- or post-measurement corrections. Our discrimination requires no statistical priors such as the ratio or number of explosives expected. The only prerequisites are three-component data and an approximate 1-D velocity model for phase windowing. Encouraging performance without local correction factors does not imply that such corrections are unimportant. In regions where sufficient data exist to calibrate local corrections, we expect that incremental but important improvements in performance are possible for a given number of stations (e.g., Wang *et al.*, 2020; Kintner *et al.*, 2020). Lastly, both methods used here are fast to calculate, making the joint method practical for near-real time screening at local scale (e.g., Dempsey *et al.*, 2020, Scafidi *et al.*, 2018).

Joint discrimination could also benefit future development of new discrimination methods, including machine-learning based techniques. The success of our application offers unique insight into the "black-box" classification resulting from machine-learning-based discrimination algorithms by highlighting specific parts of the wavefield that are diagnostic of different source types (e.g., Kortström *et al.*, 2016; Linville *et al.*, 2019; Renouard *et al.*, 2021). The high-transportability of our method may also mitigate potential challenges with network-based discriminations, where location pattern recognition or site-specific source effects could unintentionally dominate source type determination. For instance, a neural network could learn to associate explosive sources with a specific place if event location is included in end-to-end classification process along with other information such as waveforms or spectrograms (e.g., Reynen & Audet, 2017; Tang *et al.*, 2020). Our results suggest that attributes such as P/S ratios and M_L-M_C could be beneficial to include for training future classification models.

6 Conclusion

We applied P/S ratio analysis and M_L-M_C calculations to four regional datasets with ~400 small-moderate sized earthquakes and explosions recorded by tens-to-hundreds of stations concentrated at distances <200 km. The joint method requires minimal processing and little prior knowledge of site or path conditions. Joining the two discrimination methods achieves high accuracy in source type classification with individual dense local arrays (up to TPR=100% and FPR=0% when large number of stations are used). The joint method maintains similarly high performance after merging all datasets and decreasing station coverage to 8 randomly sampled stations (TPR=98.5%, TPR=4.2%). Thus, it promises transportability to other regions of interest with less favorable station coverage. Our proposed metric is suitable for reliable near-real time screening that will benefit regional monitoring and hazard evaluation, as well as future developments of machine-learning based classifiers.

Acknowledgments

All data can be downloaded via the Incorporated Research Institutions for Seismology (IRIS) Data Management Center with catalogs in the supporting information (Table S2): http://ds.iris.edu/ds/nodes/dmc/data/types/waveform-data/. The IRIS DMC is supported by the National Science Foundation under Cooperative Support Agreement EAR-1851048. Regional topography used in Figure 1 are requested from the General Bathymetric Chart of the Oceans (GEBCO; https://www.gebco.net/ last accessed August 2021). We specifically thank Eric Kiser, Lindsay Worthington, Moira Pyle, and Liang Han for the 1-D velocity models. We thank Rigobert Tibi and Chris Young for helpful discussions. The authors are grateful to the principal investigators and field workers involved in the iMUSH, BASE, SPE and SSIP projects. This research was supported by the Air Force Research Lab under contracts FA9453-17-C-0020, FA9453-19-C-0055, FA9453-20-2-0034, and FA9453-21-2-0024.

References

Anderson, D. N., Walter, W. R., Fagan, D. K., Mercier, T. M., & Taylor, S. R. (2009). Regional multistation discriminants: magnitude, distance, and amplitude corrections, and sources of error. *Bulletin of the Seismological Society of America*, *99*(2A), 794–808. https://doi.org/10.1785/0120080014

Astiz, L., Eakins, J. A., Martynov, V. G., Cox, T. A., Tytell, J., Reyes, J. C., ... & Vernon, F. L. (2014). The Array Network Facility seismic bulletin: Products and an unbiased view of United States seismicity. *Seismological Research Letters*, *85*(3), 576–593. https://doi.org/10.1785/0220130141

Bennett, T. J., & Murphy, J. R. (1986). Analysis of seismic discrimination capabilities using regional data from western United States events. *Bulletin of the Seismological Society of America*, *76*(4), 1069–1086. https://doi.org/10.1785/BSSA0760041069

Bowers, D., & Selby, N. D. (2009). Forensic seismology and the comprehensive nuclear-test-ban treaty. *Annual Review of Earth and Planetary Sciences*, *37*, 209–236. https://doi.org/10.1146/annurev.earth.36.031207.124143

Castro, R. R., Acosta, J. G., Wong, V. M., Perez-Vertti, A., Mendoza, A., & Inzunza, L. (2011). Location of aftershocks of the 4 April 2010 M w 7.2 El Mayor–Cucapah earthquake of Baja California, Mexico. *Bulletin of the Seismological Society of America*, *101*(6), 3072–3080. https://doi.org/10.1785/0120110112

Dempsey, D. E., Cronin, S. J., Mei, S., & Kempa-Liehr, A. W. (2020). Automatic precursor recognition and real-time forecasting of sudden explosive volcanic eruptions at Whakaari, New Zealand. *Nature communications*, *11*(1), 1–8. https://doi.org/10.1038/s41467-020-17375-2

Dokht, R. M., Smith, B., Kao, H., Visser, R., & Hutchinson, J. (2020). Reactivation of an intraplate fault by mine-blasting events: Implications to regional seismic hazard in Western Canada. *Journal of Geophysical Research: Solid Earth*, *125*(6), e2020JB019933. https://doi.org/10.1029/2020JB019933

Douglas, A. (2007). Forensic seismology revisited. *Surveys in Geophysics*, *28*(1), 1–31. DOI 10.1007/s10712-007-9018-7

Fawcett, T. (2006). An introduction to ROC analysis. *Pattern recognition letters*, *27*(8), 861–874. https://doi.org/10.1016/j.patrec.2005.10.010

Fisk, M. D., Gray, H. L., & MCCartor, G. D. (1996). Regional event discrimination without transporting thresholds. *Bulletin of the Seismological Society of America*, *86*(5), 1545–1558.

Fuis, G. S., Bauer, K., Goldman, M. R., Ryberg, T., Langenheim, V. E., Scheirer, D. S., ... & Aagaard, B. (2017). Subsurface geometry of the San Andreas fault in southern California: Results from the Salton Seismic Imaging Project (SSIP) and strong ground motion expectations. *Bulletin of the Seismological Society of America*, *107*(4), 1642–1662. https://doi.org/10.1785/0120160309

Gulia, L., & P. Gasperini (2021). Contamination of frequency-magnitude slope (b-value) by quarry blasts: An example for Italy, *Seismological Research Letters*. https://doi.org/10.1785/0220210080

Han, L., Hole, J. A., Stock, J. M., Fuis, G. S., Kell, A., Driscoll, N. W., ... & Lázaro-Mancilla, O. (2016). Continental rupture and the creation of new crust in the Salton Trough rift, Southern California and northern Mexico: results from the Salton Seismic Imaging Project. *Journal of Geophysical Research: Solid Earth*, *121*(10), 7469–7489. https://doi.org/10.1002/2016JB013139

Hartse, H. E., Taylor, S. R., Phillips, W. S., & Randall, G. E. (1997). A preliminary study of regional seismic discrimination in central Asia with emphasis on western China. *Bulletin of the Seismological Society of America*, *87*(3), 551–568.

Holt, M. M., Koper, K. D., Yeck, W., D'Amico, S., Li, Z., Hale, J. M., & Burlacu, R. (2019). On the portability of $\mathrm{M_L}$–$\mathrm{M_C}$ as a depth discriminant for small seismic events recorded at local distances. *Bulletin of the Seismological Society of America*, *109*(5), 1661–1673. https://doi.org/10.1785/0120190096

Kim, W. Y., Simpson, D. W., & Richards, P. G. (1993). Discrimination of earthquakes and explosions in the eastern United States using regional high-frequency data. *Geophysical research letters*, *20*(14), 1507–1510. https://doi.org/10.1029/93GL01267

Kintner, J. A., Michael Cleveland, K., Ammon, C. J., & Nyblade, A. (2020). Testing a local-distance *Rg/Sg* discriminant using observations from the Bighorn Region, Wyoming. *Bulletin of the Seismological Society of America*, *110*(2), 727–741. https://doi.org/10.1785/0120190188

Koper, K. D., Holt, M. M., Voyles, J. R., Burlacu, R., Pyle, M. L., Wang, R., & Schmandt, B. (2021). Discrimination of small earthquakes and buried single-fired chemical explosions at local sistances (<150 km) in the Western United States from comparison of local magnitude (M_L) and coda duration magnitude (M_C). *Bulletin of the Seismological Society of America*, *111*(1), 558–570. https://doi.org/10.1785/0120200188

Kortström, J., Uski, M., & Tiira, T. (2016). Automatic classification of seismic events within a regional seismograph network. *Computers & Geosciences*, *87*, 22–30. https://doi.org/10.1016/j.cageo.2015.11.006

Linville, L., Pankow, K., & Draelos, T. (2019). Deep learning models augment analyst decisions for event discrimination. *Geophysical Research Letters*, *46*(7), 3643–3651. https://doi.org/10.1029/2018GL081119

Mackey, K. G., Fujita, K., Gounbina, L. V., Koz'min, B. M., Imaev, V. S., Imaeva, L. P., & Sedov, B. M. (2003). Explosion contamination of the northeast Siberian seismicity catalog: Implications for natural earthquake distributions and the location of the Tanlu fault in Russia. *Bulletin of the Seismological Society of America*, *93*(2), 737–746. https://doi.org/10.1785/0120010196

Marzen, R. E., Gaherty, J. B., Shillington, D. J., & Kim, W. Y. (2021). Shaking in the Southeastern United States: Examining earthquakes and blasts in the Central Georgia–South Carolina Seismic Region. *Seismological Research Letters*. https://doi.org/10.1785/0220210029

O'Rourke, C. T., Baker, G. E., & Sheehan, A. F. (2016). Using P/S amplitude ratios for seismic discrimination at local distances. *Bulletin of the Seismological Society of America*, *106*(5), 2320–2331. https://doi.org/10.1785/0120160035

O'Rourke, C. T., & Baker, G. E. (2017). A spectrogram-based method of Rg detection for explosion monitoring. *Bulletin of the Seismological Society of America*, *107*(1), 34–42. https://doi.org/10.1785/0120160184

Pechmann, J. C., Bernier, J. C., Nava, S. J., & Terra, F. M. (2006). Correction of systematic time-dependent coda magnitude errors in the Utah and Yellowstone National Park region earthquake catalogs, 1981–2001, in Integrated Regional and Urban Seismic Monitoring—Wasatch Front Area, Utah and Adjacent Intermountain Seismic Belt, W. J. Arabasz, R. B. Smith, J. C. Pechmann, K. L. Pankow, and R. Burlacu (Editors), Appendix C, U.S. Geol. Surv. Final Tech. Rept. Cooperative Agreement 04HQAG0014, 137 pp., available at https://earthquake.usgs.gov/cfusion/external_grants/reports/04HQAG0014.pdf(last accessed August 2021).

Pyle, M. L., & Walter, W. R. (2019). Investigating the effectiveness of P/S amplitude ratios for local distance event discrimination. *Bulletin of the Seismological Society of America*, *109*(3), 1071–1081. https://doi.org/10.1785/0120180256

Rabin, N., Bregman, Y., Lindenbaum, O., Ben-Horin, Y., & Averbuch, A. (2016). Earthquake-explosion discrimination using diffusion maps. *Geophysical Journal International*, *207*(3), 1484–1492. https://doi.org/10.1093/gji/ggw348

Renouard, A., Maggi, A., Grunberg, M., Doubre, C. and Hibert, C. (2021). Toward false event detection and quarry blast versus earthquake discrimination in an operational setting using semiautomated machine learning. *Seismological Research Letters*. https://doi.org/10.1785/0220200305

Reynen, A., & Audet, P. (2017). Supervised machine learning on a network scale: Application to seismic event classification and detection. *Geophysical Journal International*, *210*(3), 1394–1409. https://doi.org/10.1093/gji/ggx238

Richter, C.F (1958). *Elementary Seismology*, W.H. Freeman and Co., San Francisco, California, 768 pp.

Rodgers, A. J., Walter, W. R., Schultz, C. A., Myers, S. C., & Lay, T. (1999). A comparison of methodologies for representing path effects on regional P/S discriminants. *Bulletin of the Seismological Society of America*, *89*(2), 394–408.

Russell, D. R. (2006). Development of a time-domain, variable-period surface-wave magnitude measurement procedure for application at regional and teleseismic distances, part I: Theory. *Bulletin of the Seismological Society of America*, *96*(2), 665–677. https://doi.org/10.1785/0120050055

Scafidi, D., Viganò, A., Ferretti, G., & Spallarossa, D. (2018). Robust picking and accurate location with RSNI-Picker2: Real-time automatic monitoring of earthquakes and nontectonic events. *Seismological Research Letters*, *89*(4), 1478–1487. https://doi.org/10.1785/0220170206

Selby, N. D., Marshall, P. D., & Bowers, D. (2012). mb: Ms event screening revisited. *Bulletin of the Seismological Society of America, 102*(1), 88–97. https://doi.org/10.1785/0120100349

Snelson, C. M., Abbott, R. E., Broome, S. T., Mellors, R. J., Patton, H. J., Sussman, A. J., ... & Walter, W. R. (2013). Chemical explosion experiments to improve nuclear test monitoring. *Eos, Transactions American Geophysical Union*, *94*(27), 237–239. https://doi.org/10.1002/2013EO270002

Stanley, W. D., Johnson, S. Y., Qamar, A. I., Weaver, C. S., & Williams, J. M. (1996). Tectonics and seismicity of the southern Washington Cascade Range. *Bulletin of the Seismological Society of America*, *86*(1A), 1–18.

Stevens, J. L., & Day, S. M. (1985). The physical basis of *mb*:*Ms* and variable frequency magnitude methods for earthquake/explosion discrimination. *Journal of Geophysical Research: Solid Earth*, *90*(B4), 3009–3020. https://doi.org/10.1029/JB090iB04p03009

Stump, B. W., Hedlin, M. A., Pearson, D. C., & Hsu, V. (2002). Characterization of mining explosions at regional distances: Implications with the international monitoring system. *Reviews of Geophysics*, *40*(4), 1011. https://doi.org/10.1029/1998RG000048

Tang, L., Zhang, M., & Wen, L. (2020). Support vector machine classification of seismic events in the Tianshan orogenic belt. *Journal of Geophysical Research:*

Solid Earth, *125*(1), e2019JB018132. https://doi.org/10.1029/2019JB018132

Taylor, S. R., Denny, M. D., Vergino, E. S., & Glaser, R. E. (1989). Regional discrimination between NTS explosions and western US earthquakes. *Bulletin of the Seismological Society of America*, *79*(4), 1142–1176. https://doi.org/10.1785/BSSA0790041142

Tian, D., Yao, J., & Wen, L. (2018). Collapse and earthquake swarm after North Korea's 3 September 2017 nuclear test. *Geophysical Research Letters*, *45*(9), 3976–3983. https://doi.org/10.1029/2018GL077649

Tibi, R. (2021). Discrimination of seismic events (2006–2020) in North Korea using P/Lg amplitude ratios from regional stations and a bivariate discriminant function. *Seismological Research Letters*. *92* (4), 2399–2409. https://doi.org/10.1785/0220200432

Ulberg, C. W., Creager, K. C., Moran, S. C., Abers, G. A., Thelen, W. A., Levander, A., ... & Crosson, R. S. (2020). Local source Vp and Vs tomography in the Mount St. Helens region with the iMUSH broadband array. *Geochemistry, Geophysics, Geosystems*, *21*(3), e2019GC008888. https://doi.org/10.1029/2019GC008888

Voyles, J. R., Holt, M. M., Hale, J. M., Koper, K. D., Burlacu, R., & Chambers, D. J. (2020). A new catalog of explosion source parameters in the Utah region with application to M_L–M_C-based depth discrimination at local distances. *Seismological Research Letters*, *91*(1), 222–236. https://doi.org/10.1785/0220190185

Walter, W. R., Mayeda, K. M., & Patton, H. J. (1995). Phase and spectral ratio discrimination between NTS earthquakes and explosions. Part I: Empirical observations. *Bulletin of the Seismological Society of America*, *85*(4), 1050–1067.

Walter, W. R., & Taylor, S. R. (2001). A revised magnitude and distance amplitude correction (MDAC2) procedure for regional seismic discriminants: Theory and testing at NTS (No. UCRL-ID-146882). Lawrence Livermore National Lab.(LLNL), Livermore, CA (United States). https://doi.org/10.2172/15013384

Walter, W. R., Dodge, D. A., Ichinose, G., Myers, S. C., Pasyanos, M. E., & Ford, S. R. (2018). Body-wave methods of distinguishing between explosions, collapses, and earthquakes: Application to recent events in North Korea. *Seismological Research Letters, 89*(6), 2131–2138. https://doi.org/10.1785/0220180128

Wang, R., Schmandt, B., & Kiser, E. (2020). Seismic discrimination of controlled explosions and earthquakes near Mount St. Helens using P/S ratios. *Journal of Geophysical Research: Solid Earth*, *125*(10), e2020JB020338. https://doi.org/10.1029/2020JB020338

Wang, T., Bian, Y., Yang, Q., & Ren, M. (2021). Correction of P/S amplitude ratios for low-magnitude seismic events based on Bayesian kriging method. *Bulletin of the Seismological Society of America.* https://doi.org/10.1029/2020JB020338

Worthington, L. L., Miller, K. C., Erslev, E. A., Anderson, M. L., Chamberlain, K. R., Sheehan, A. F., ... & Siddoway, C. S. (2016). Crustal structure of the Bighorn Mountains region: Precambrian influence on Laramide shortening and uplift in north-central Wyoming. *Tectonics*, *35*(1), 208–236. https://doi.org/10.1002/2015TC003840

Zeiler, C., & Velasco, A. A. (2009). Developing local to near-regional explosion and earthquake discriminants. *Bulletin of the Seismological Society of America*, *99*(1), 24–35. https://doi.org/10.1785/0120080045

References from supporting information

Anderson, M. L., & Myers S. C. (2010). Assessment of regional-distance location calibration using a multiple-event location algorithm. *Bulletin of the Seismological Society of America*, *100*(2), 868–875, https://doi.org/10.1785/0120090145

Brocher, T. M. (2005). Empirical relations between elastic wave speeds and density in the Earth's crust. *Bulletin of the seismological Society of America*, *95*(6), 2081–2092. https://doi.org/10.1785/0120050077

Kennett, B. L., Engdahl, E. R., & Buland, R. (1995). Constraints on seismic velocities in the Earth from traveltimes. *Geophysical Journal International*, *122*(1), 108–124. https://doi.org/10.1111/j.1365-246X.1995.tb03540.x

Kiser, E., Palomeras, I., Levander, A., Zelt, C., Harder, S., Schmandt, B., ... & Ulberg, C. (2016). Magma reservoirs from the upper crust to the Moho inferred from high-resolution Vp and Vs models beneath Mount St. Helens, Washington State, USA. *Geology*, *44*(6), 411–414. https://doi.org/10.1130/G37591.1

Tibi, R., Koper, K. D., Pankow, K. L., & Young, C. J. (2018). Discrimination of anthropogenic events and tectonic earthquakes in Utah using a quadratic discriminant function approach with local distance amplitude ratios. *Bulletin of the Seismological Society of America*, *108*(5A), 2788–2800. https://doi.org/10.1785/0120180024

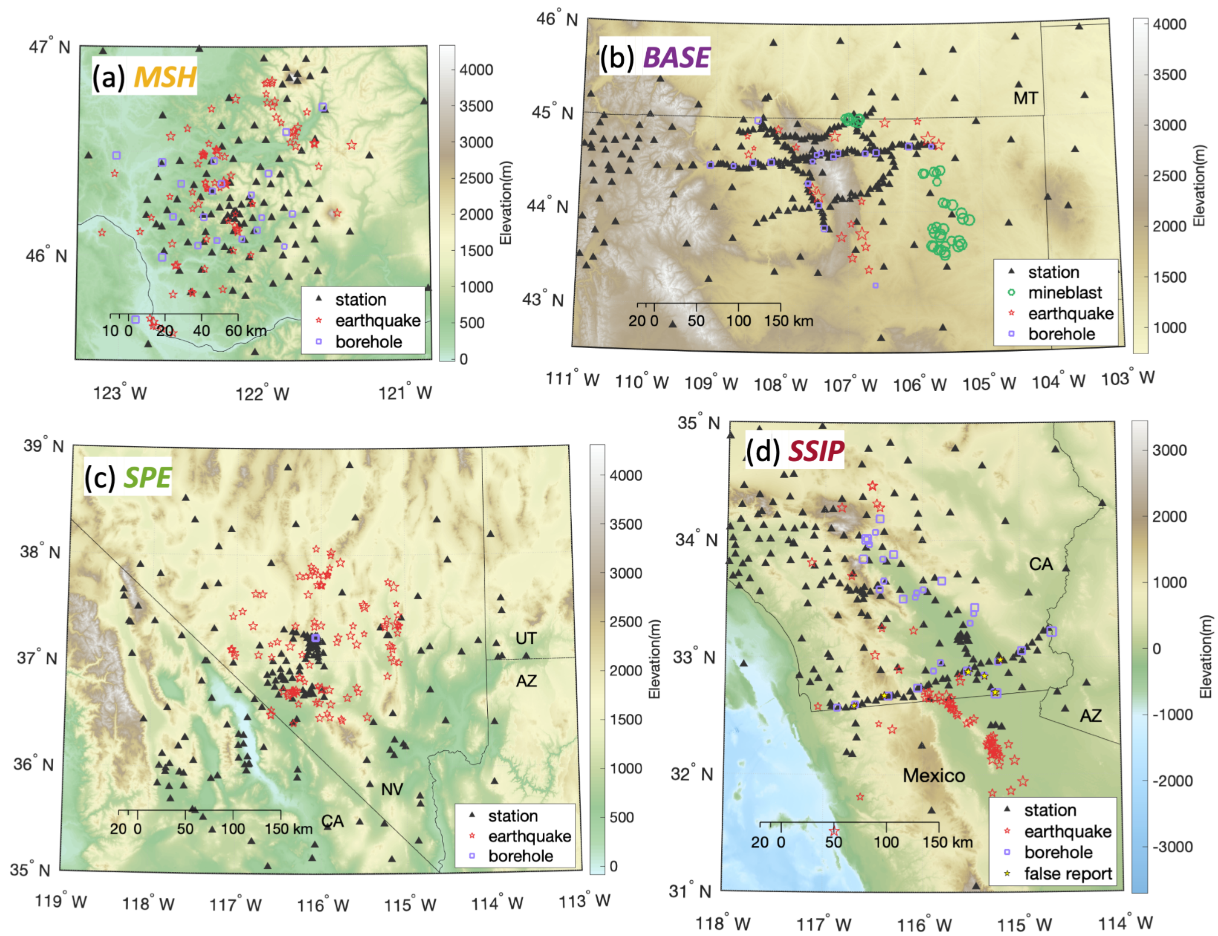

Figure 1. Seismic networks and events for the four studied regions (a–d). See Table S1 for details of the six "false report" earthquakes in SSIP (d).

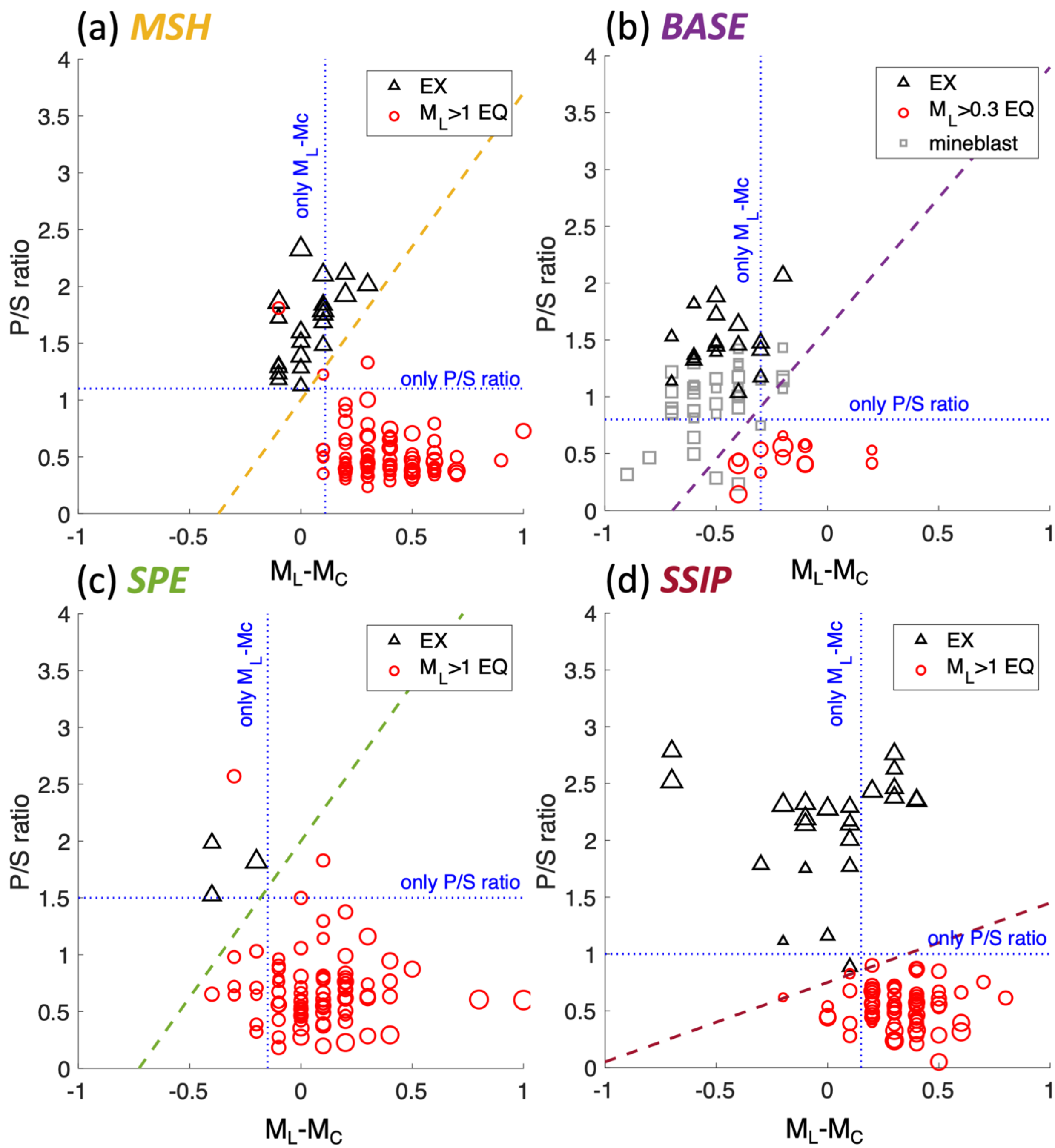

Figure 2. The four datasets analyzed in the joint domain. The horizontal and vertical dotted lines are best P/S ratio and M_L-M_C cutoffs, respectively. The diagonal dashed lines are optional joint cutoffs resolved via grid searching (see

Figure S6). For BASE, the results of 37 mine blasts are shown but excluded from further analysis.

Dataset	**MSH**	**BASE**	**SPE**	**SSIP**
Neq	90	14	88	70
Nex	22	19	3	22
P/S	**1.1**	**0.9–1.1**	**1.5**	**1**
TPR (recall)	1	1	1	0.96
FPR	0.03	0	0.02	0
precision	0.88	1	0.60	1
M_L-M_C	**0.11**	**-0.3**	**-0.15**	**0.15**
TPR (recall)	0.86	0.89	1	0.71
FPR	0.07	0.21	0.11	0.11
precision	0.76	0.85	0.23	0.68
Joint	**[2.70 1.00]**	**[2.30 1.60]**	**[2.75 2.00]**	**[0.70 0.75]**
TPR (recall)	1	1	1	1
FPR	0.01	0	0.01	0
precision	0.96	1	0.75	1

Table 1. Best discrimination performances for three metrics: 1. P/S; 2. M_L-M_C; and 3. Joint, where numbers in brackets are slope and intercept. For all cases, "explosive" is defined as "positive" (P). True Positive Rate-TPR (recall): TP/(TP+FN); False Positive Rate-FPR: FP/(FP+TN); Precision: TP/(FP+TP). Neq and Nex are final numbers of earthquakes and explosives that have both valid P/S and M_L-M_C measurements.

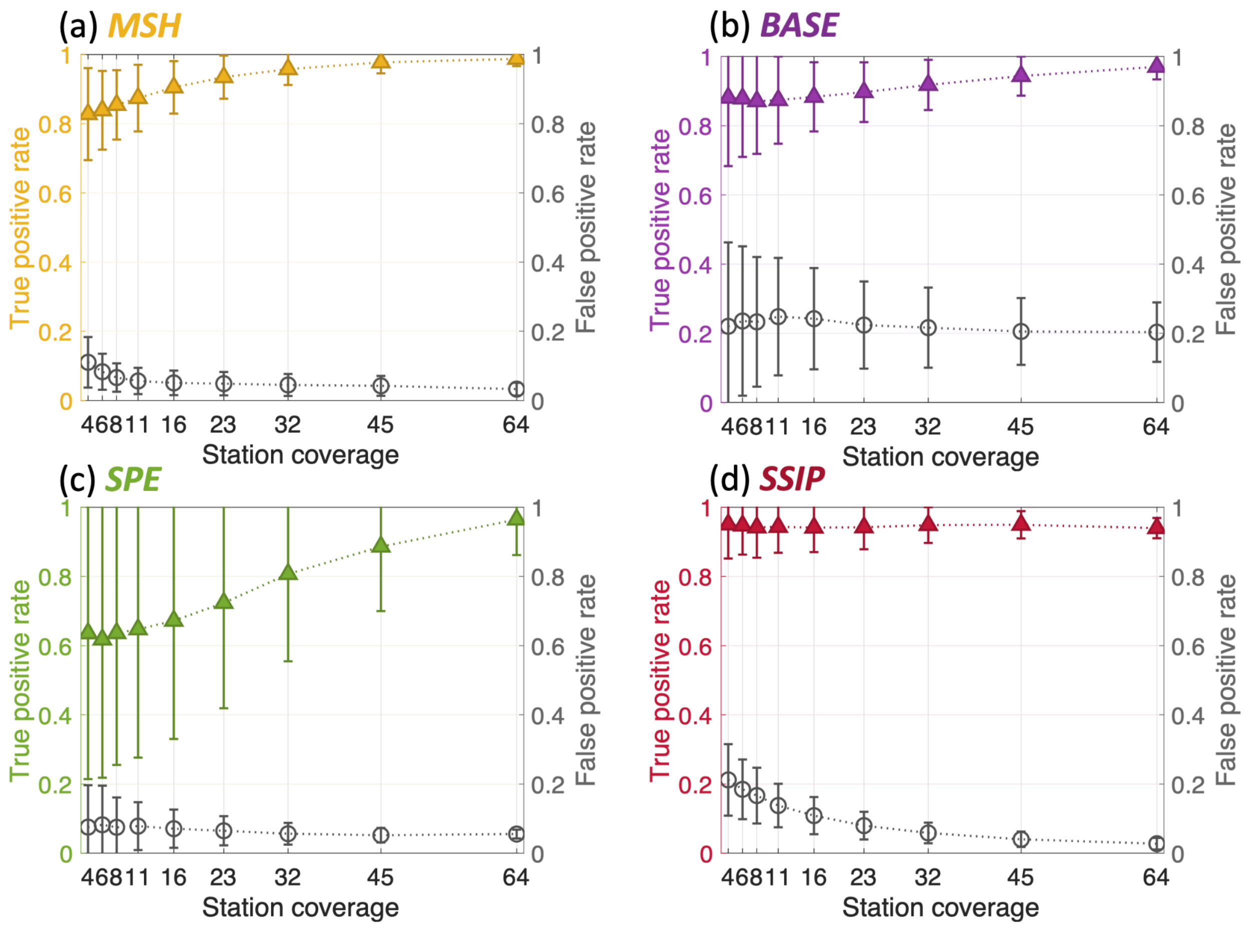

Figure 3. Station coverage test for the four datasets (as labeled). Only broad-band stations (i.e., “HH” and “BH”) are considered in BASE. Error bars indicate the standard deviations from 1,000 trials.

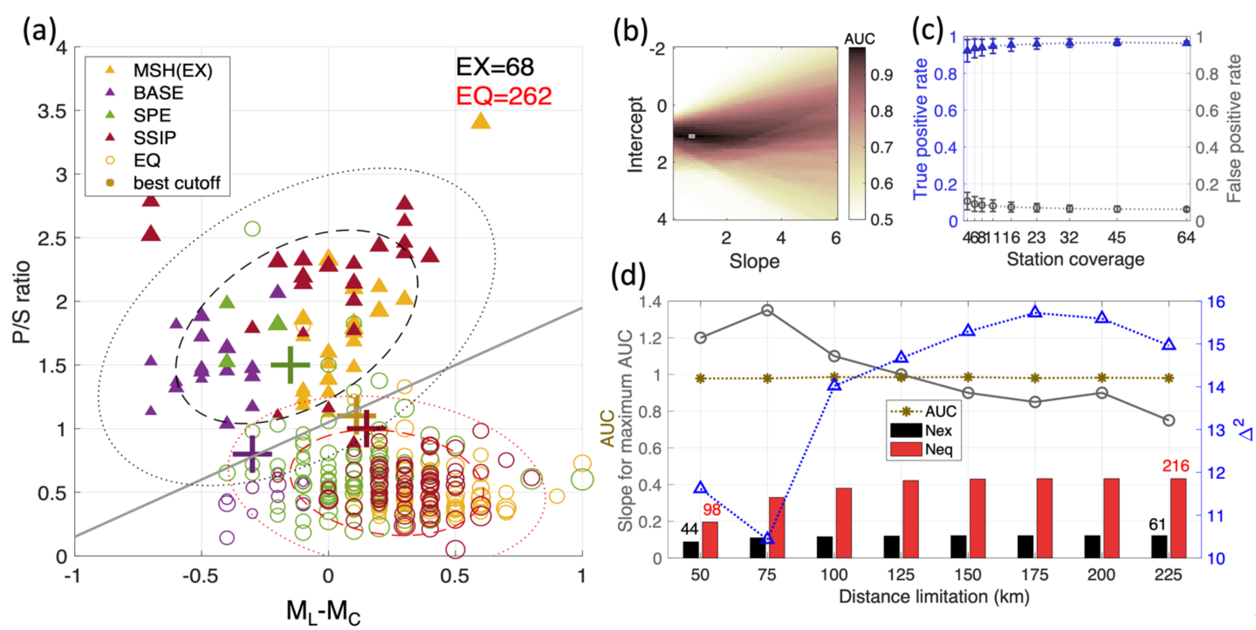

Fi

4. Discrimination results in the joint domain for merged dataset. (a) All event-based P/S or M_L-M_C of the four datasets as labeled. The cross symbols mark the best P/S and M_L-M_C cut offs for each dataset (see Figure 2). The dashed and dotted ellipses are the covariance of one and two standard deviations, respectively. The grey line marks the best joint discrimination threshold determined from a grid search for maximum AUC shown in (b). (c) Station coverage test for the merged dataset. (d) Slope and discrimination performance variation (Δ^2 and AUC) with source-station distance limitations. Red (Neq) and black (Nex) bars are the numbers of events surviving at each distance limit; only the nearest and farthest distance are labeled with numbers for scaling.

AGU PUBLICATIONS

Geophysical Research Letters

Supporting Information for

Advancing Local Distance Discrimination of Explosions and Earthquakes with Joint P/S and M_L-M_C Classification

Ruijia Wang[1,2], Brandon Schmandt[1], Monique Holt[3,4], and Keith Koper[3]

1.Department of Earth & Planetary Sciences, University of New Mexico, Albuquerque, NM, US

2.Department of Earth and Space Sciences, Southern University of Science and Technology, Shenzhen, Guangdong, China

3.Department of Geology and Geophysics, University of Utah, Salt Lake City, Utah, US

4.Department of Earth and Environmental Sciences, University of Illinois at Chicago, Chicago, Illinois, US

Contents of this file

Text S1 to S4
Figures S1 to S9
Table S1

Additional Supporting Information (Files uploaded separately)

Caption for Table S2

Introduction

The supporting information provides details for the local velocity models (Text S1 and Figure S1), datasets (Figure S2–S3, Figure S8–9, also see Table S2 uploaded separately), and processing parameters (Text S2–S3 and Figures S3–S6). The P/S ratio results for SSIP using 3-sec windows are discussed in Text S3 and shown in Figure S4. The optimal P/S ratio and M_L-M_C cutoffs of four datasets are determined based on Area Under the Curve (AUC) from Receiver Operating Characteristic curves (ROC, Figure S5). Figure S6 shows the determination of the best "combined" line by searching over intercept and slopes in the P/S vs. M_L-M_C domain, where best line(s) are chosen based on the maximum AUC. Figure S7 illustrates how the separation of the two populations decreases with station coverage. Figure S8 shows an example of the joint discrimination of the merged dataset with limited station distances (<100 km). Figure S9 includes events that failed quality control (e.g., insufficient M_L or M_C measurements).

Text S1. 1-D Velocity models for the four regions

The 1-D velocity model for MSH is adopted from Kiser *et al.* (2016), where the P and S phases were manually picked from ~3,000 geophones during the controlled source survey (the geophone records are not used in this study). For BASE, we averaged and smoothed the 3D velocity model from Worthington *et al*. (2016) to create the 1-D velocity model for phase prediction. The 1-D velocity model for SPE is adopted from Anderson & Myers (2010). The starting 1-D velocity model of the regional imaging project (Han *et al.*, 2016) is used for SSIP. We merge the crustal models with ak135 (Kennett *et al.*, 1995) at deeper depths (i.e., below the Moho). Lastly, we use the empirical equation from Brocher (2005) to calculate S-wave velocity or density when they are not provided in the original models (Figure S1).

Text S2. Parameter details for P/S ratio calculations and differences to previous studies

Several parameters of P/S calculation and performance evaluation may contribute to our discrimination results:

The P and S phase arrivals are calculated using the corresponding velocity models. The phase windows are scaled with the predicted arrival time differences ($dt = tp - ts$) with two constraints: 1) where 5%dt before and 50%dt after the phases are used; 2) total window lengths between 1–3 sec. In other words, we removed records with phase windows less than 1 sec to avoid potential contamination from phase picking uncertainties. Records at larger distances (~>50km) have a uniform length of 3 sec. The 5%dt buffer window (up to 0.3 sec) before the arrivals is included to mitigate the effects of potential late phase predictions.

As most of the broadband stations have a sampling rate of 40 Hz, we adopted the relatively high and wide frequency band (10–18 Hz) for local distances from Wang *et al*. (2020). Considering our window choices, all phase energy calculations contain at least 10 periods at 10–18 Hz. We refer readers to Wang *et al.* (2020) for more comprehensive and detailed analysis on parameter optimizations (e.g., component, phase window sizes, and frequency band).

In addition to windowing & frequency choices, our method of P/S calculation is different from previous regional studies (e.g., O'Rourke *et al.*, 2016) in a few aspects: 1) all three components are used to calculate phase energy, including transverse for P-waves; 2) no pre-S noise window or S-wave SNR is used; and 3) no MDAC corrections were applied. Such modifications accommodate high-scattering, potential P-coda contamination (to S waves), as well as unsuitable larger-scale corrections at near-distances.

Lastly, our performance evaluation is event-oriented, where TPR and FPR are used instead of variances (e.g., standard deviation from L2 norm; or median absolute deviation from L1 norm). The TPR and FPR (and AUC; or recall and precision) parameters are more resistant to outliers, analogous to event-based L1-norm evaluations. In contrast and for a comparison, the covariance ellipses of the two populations overlap at two standard deviations in the P/S vs. M_L-M_C domain (Figure S7 and S8, also see Figure 4 I the main text). For record-based P/S ratios, the distributions for earthquakes and explosions overlap across most distances like previous studies, even when median absolute deviation is used (Figure S3).

Text S3. P/S ratios for SSIP calculated with 3-sec windows

Considering the significant variation of both topography and Moho depths (Han *et al.*, 2016) in southern California, a slightly wider window (4 sec instead of 3 sec) is used during P/S ratio analysis to account for potential inaccuracies of phase prediction from 1-D velocity model. The 3-sec windows lead to slightly worse discrimination (Figure S4) than 4-sec ones (Figure S3d). We obtained TPR=95.13% and FPR=5.71% with maximum AUC=0.9470 at a P/S cutoff of 0.9. For comparison, when 4-sec phase windows are used, we achieved TPR=97.56% and FPR=0.00% with maximum AUC=0.9818. The number of records also increased (2431 vs. 2754) using 4-sec, suggesting more records reach SNR>2 and a better capture of P energies in the predicted phase windows. Therefore, the modified window (4-sec) is used for our analysis throughout the main text for SSIP. Other datasets are evaluated with 3-sec windows.

Text S4. Mahalanobis distances (Δ^2) from Multivariate Quadratic Discriminant Function (QDF)

This section introduce the revised Mahalanobis distance calculated from the multivariate quadratic discriminant function (QDF).
For a given sampled event (earthquake or borehole shot), the measured discrimination vector $\boldsymbol{r}$ contains two elements:

$$\boldsymbol{r} = (d_1, d_2)^T, \tag{1}$$

Where, $d_1 = log10(P/S)$, is the array-median P/S ratio and $d_2 = M_L - Mc$ is the array-median magnitude difference. Following Tibi *et al.* (2018) and Tibi (2021), we use the P/S ratio in log scale to ensure they are roughly at comparable range with M_L-M_C. The bivariate Quadratic Discriminant Function (QDF) is then calculated by

$$D(\boldsymbol{r}) = \boldsymbol{r}^T\boldsymbol{A}\boldsymbol{r} + \boldsymbol{B}\boldsymbol{r} + k, \tag{2}$$

in which

$$\boldsymbol{A} = -\frac{1}{2}(\boldsymbol{S}_{\boldsymbol{ex}}^{-1} - \boldsymbol{S}_{\boldsymbol{eq}}^{-1})^T, \tag{3}$$

$$\boldsymbol{B} = \boldsymbol{\mu}_{\boldsymbol{ex}}^T\boldsymbol{S}_{\boldsymbol{ex}}^{-1} - \boldsymbol{\mu}_{\boldsymbol{eq}}^T\boldsymbol{S}_{\boldsymbol{eq}}^{-1}, \tag{4}$$

$$k = -\frac{1}{2}\left[\ln\left(\frac{|S_{ex}|}{|S_{eq}|}\right) + \left(\boldsymbol{\mu}_{\boldsymbol{ex}}^T\boldsymbol{S}_{\boldsymbol{ex}}^{-1}\boldsymbol{\mu}_{\boldsymbol{ex}} - \boldsymbol{\mu}_{\boldsymbol{eq}}^T\boldsymbol{S}_{\boldsymbol{eq}}^{-1}\boldsymbol{\mu}_{\boldsymbol{eq}}\right)\right], \tag{5}$$

Where, $\boldsymbol{\mu}_{\boldsymbol{ex}}$is the mean of $\boldsymbol{R}_{\boldsymbol{ex}} = [\boldsymbol{r}_{\boldsymbol{1}}\ \boldsymbol{r}_{\boldsymbol{2}}\ \boldsymbol{r}_{\boldsymbol{3}} \ldots \boldsymbol{r}_{\boldsymbol{n}}]$ that contains all discrimination vectors for n explosive events; and $\boldsymbol{S}_{\boldsymbol{ex}}$ is the 2×2 ratio covariance matrix for $\boldsymbol{R}_{\boldsymbol{ex}}$. The vectors and matrices with "$\boldsymbol{eq}$" subscripts are defined correspondingly. For a given event, the discrimination score (D) is expected to be positive for explosive sources and negative for earthquakes. The Mahalanobis distance between the two types of events is defined as:

$$\Delta^2 = D(\boldsymbol{\mu}_{\boldsymbol{ex}}) - D(\boldsymbol{\mu}_{\boldsymbol{eq}}) \tag{6}$$

Taking covariances into consideration, Mahalanobis distance (Δ^2) is a quantitative measure of the "closeness" between two populations in the joint domain (e.g., Figure S6). Lastly, the minimum probability of misclassification P_M, is then calculated using the Mahalanobis distance:

$$P_M = \frac{1}{\sqrt{2\pi}}\int_{-\infty}^{-\Delta/2} e^{-x^2/2}\, dx\ , \tag{7}$$

To evaluate the performance of joint method, only events that have both array-median P/S ratio and M_L-M_C are carried over for the joint discrimination. Thus, the total number (n) of explosives and earthquakes are 68 and 262, respectively. Events that failed to meet the criterion (<3 station-based measurements) are shown Figure S9.

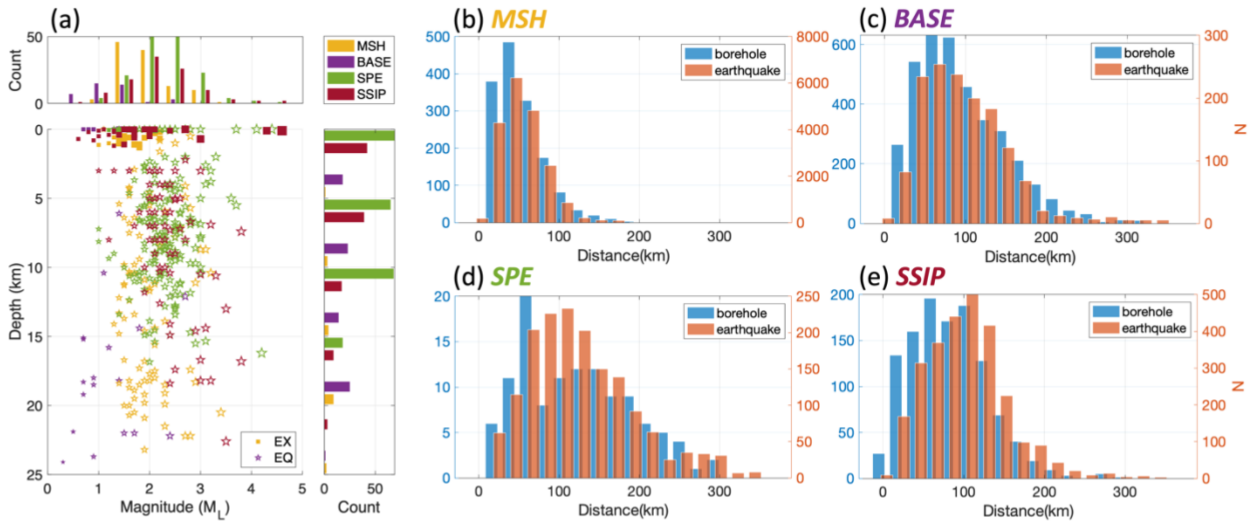

Figure S1. a) Magnitude and event depth distributions for the four datasets (see Figure 1). b–e) event-station distance distributions. EX-explosives (borehole events), EQ-earthquakes.

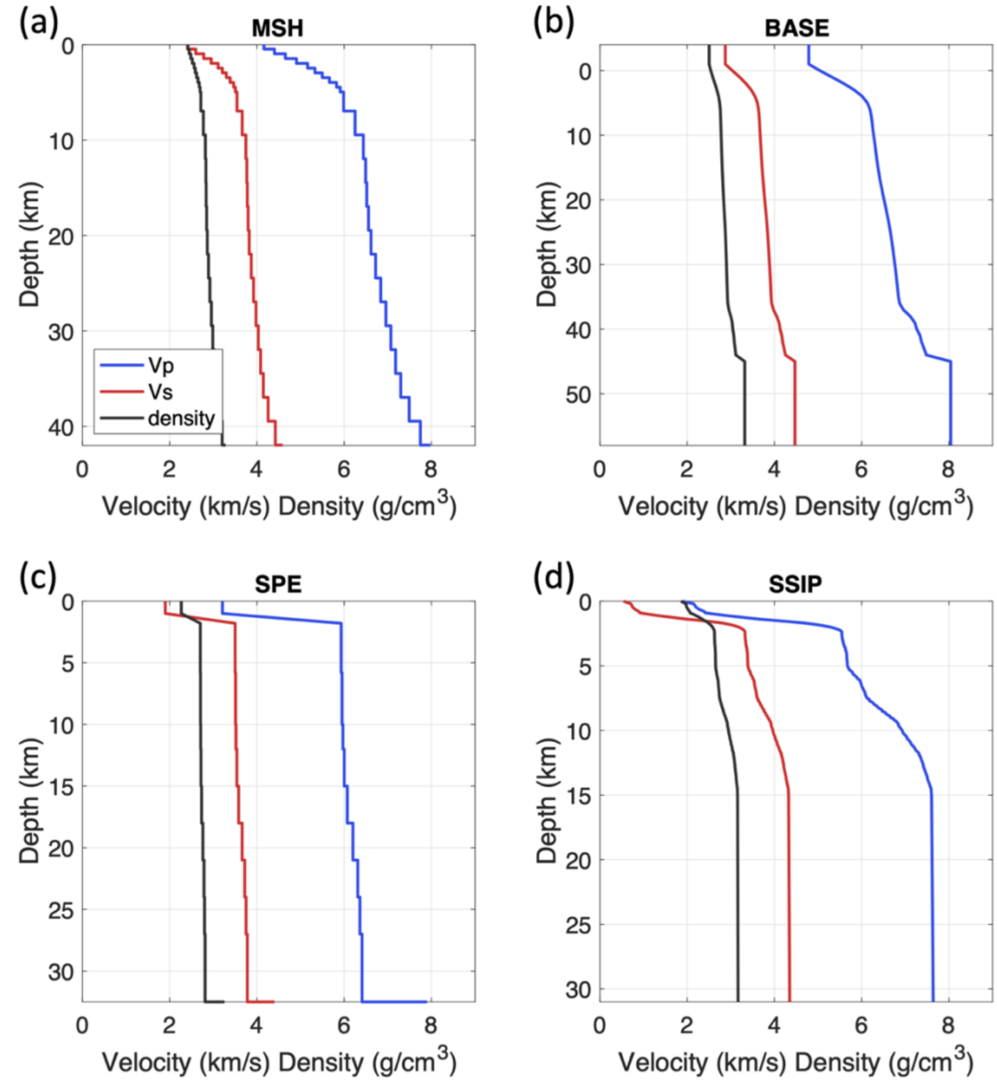

Figure S2. Velocity models used for the four study regions (see Figure 1 in main text).

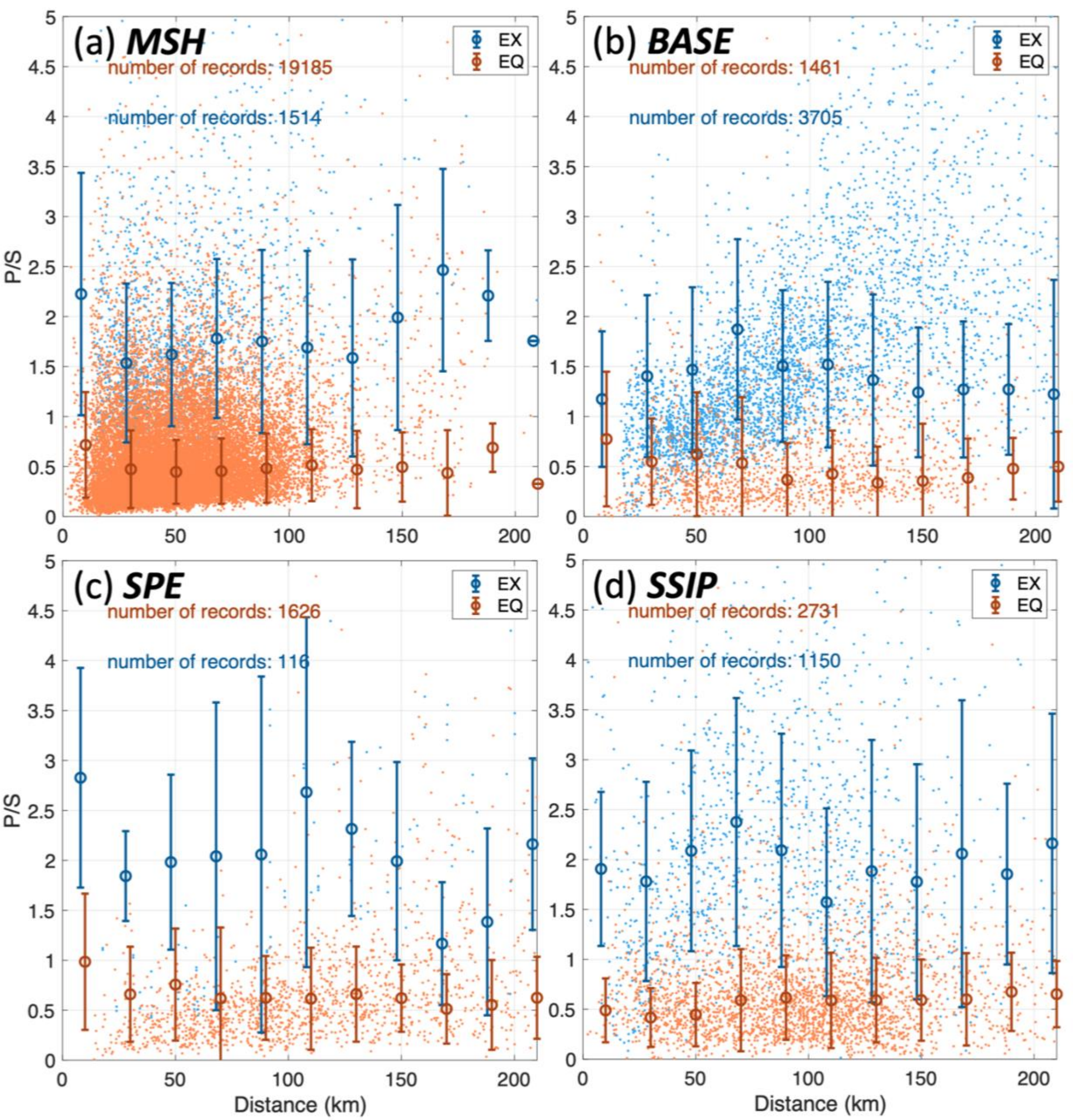

Figure S3. P/S ratio dependence on distances. Distances beyond 200 km are used for calculations but not shown for consistency. The bold bars are average and median absolute deviation for each 20-km bin. EX-explosives (borehole events), EQ-earthquakes.

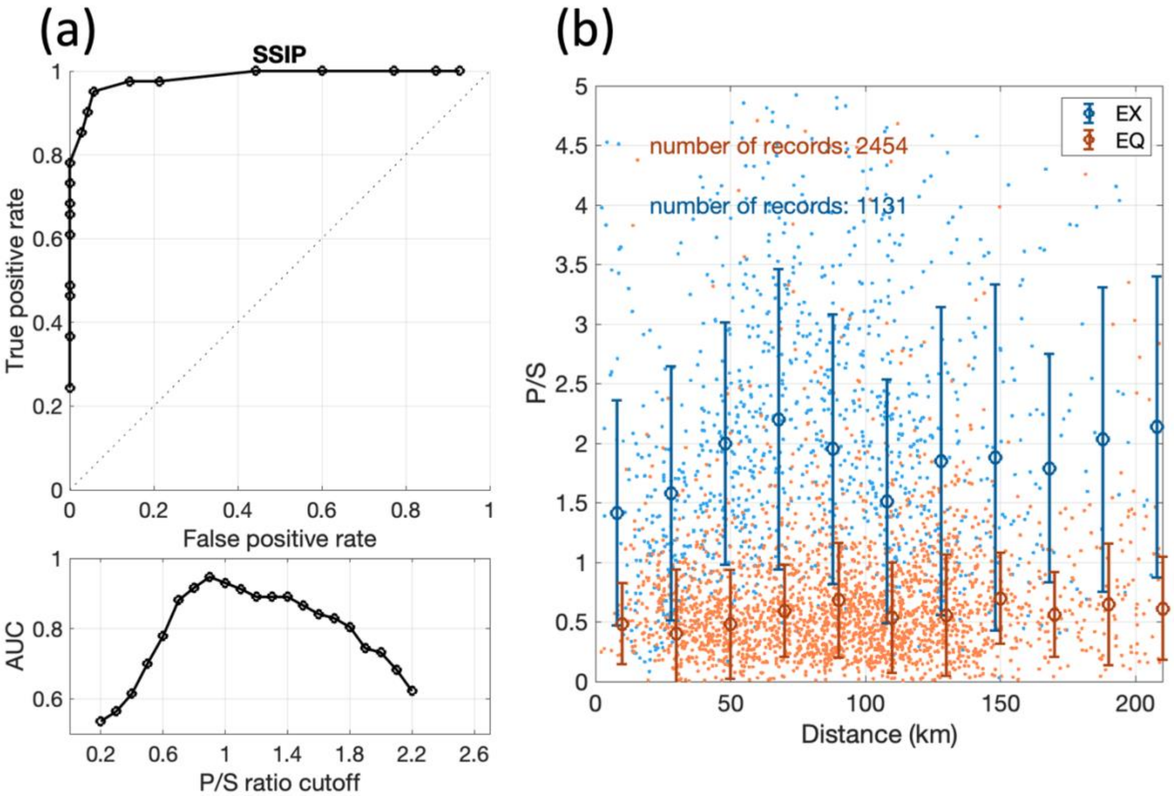

Figure S4. P/S calculation results for SSIP with 3-sec phase windows. a) ROC and AUC curves. Note that the best P/S cutoff peaks at 0.9 instead of 1 (4-sec). b) same as Figure S3d but for 3-sec windows. Note the number of records is lower.

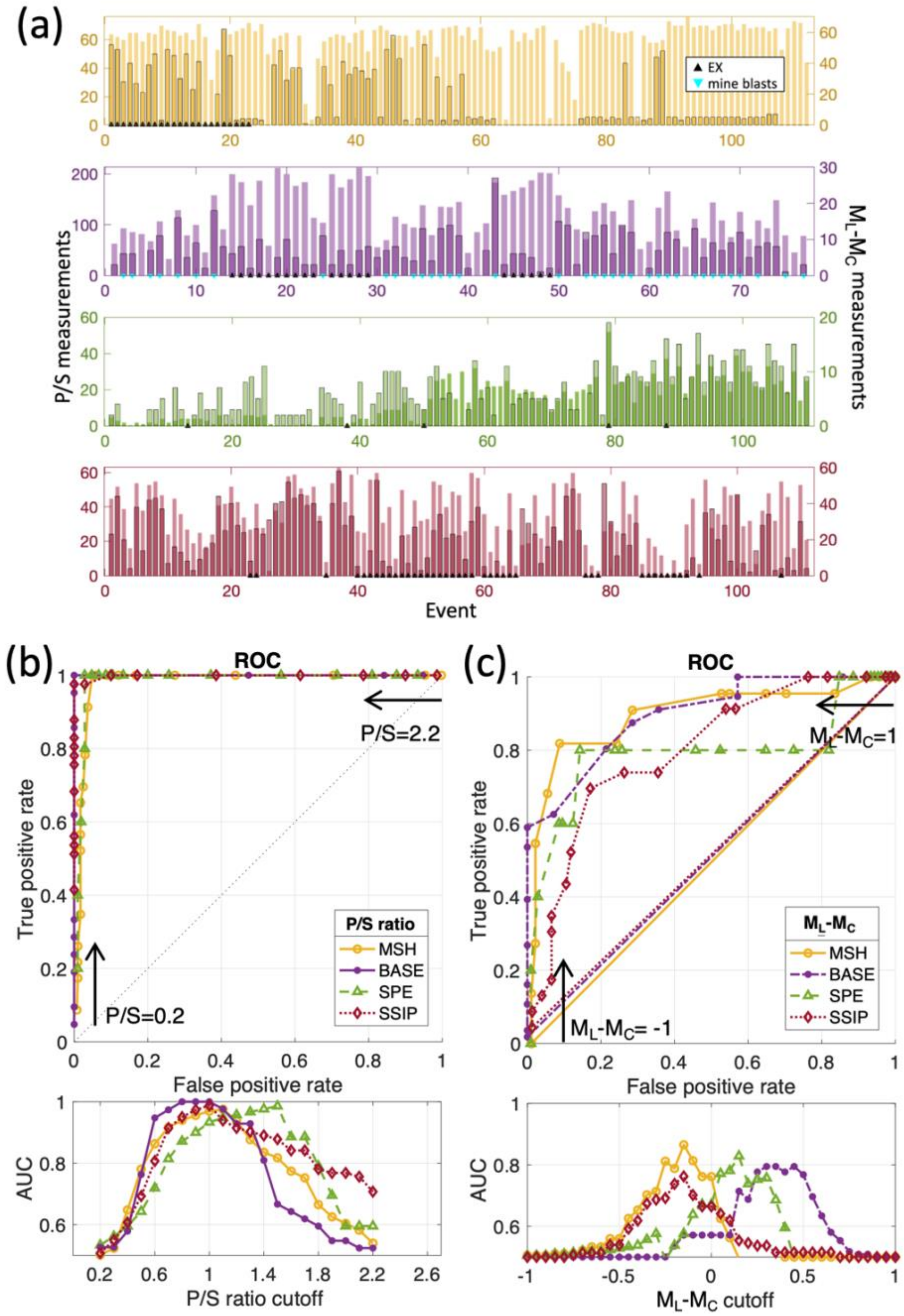

Figure S5. a) Valid number of measurements for both methods (top to bottom, MSH, BASE, SPE, SSIP) . Performance evaluation and best cutoff thresholds for P/S ratio (b) and M_L-M_C (c). Here the TPR and FPR are slightly different from Table 1 in the main text, as events with only valid P/S or M_L-M_C are counted in. In the other word, we do not require an event to have both measurements in this case; Table 1 is showing statistics obtained from the intersection dataset of b) and c). The bottom panels showing AUC as a function of cutoff value are derived by calculating the AUC based on a 3-point curve connecting the lower left corner, the FPR and TPR performance coordinate, and the upper right corner.

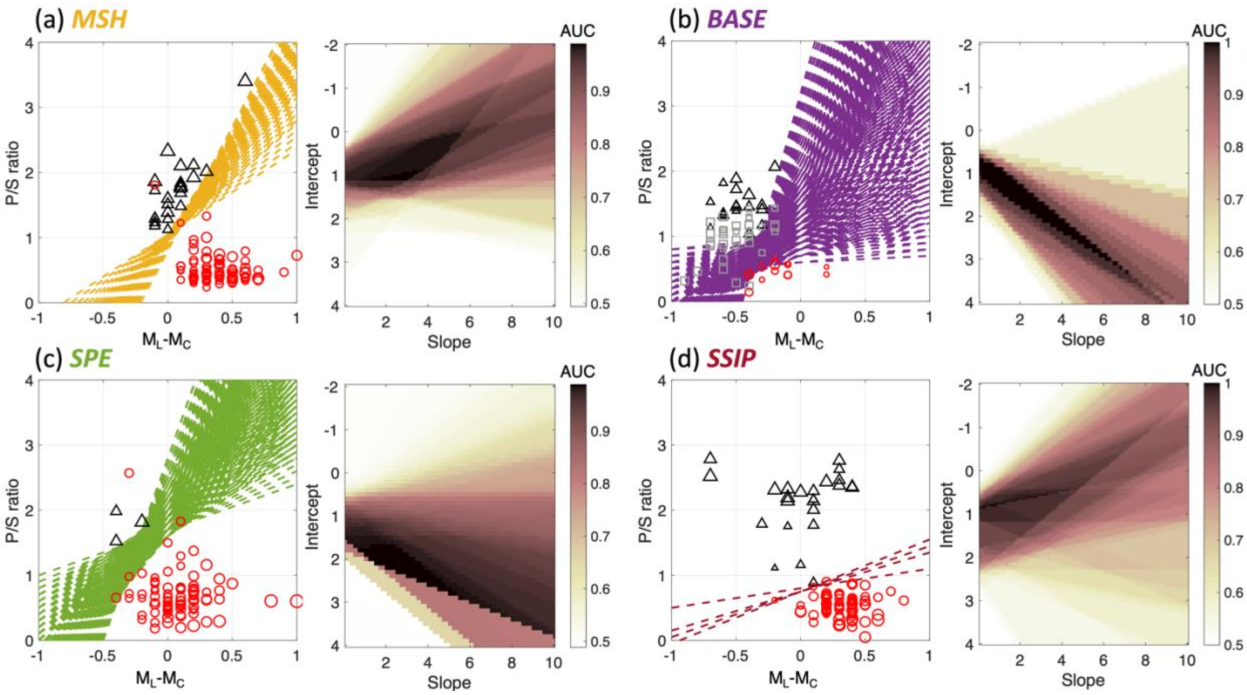

Figure S6. Grid search of slopes and intercepts for the best discrimination “combined” line for the four studied datasets. The color bars are areas under the curve (AUC) from the 2-D ROC analysis. The dashed lines are the combinations of slopes and intercepts that achieve the highest AUCs.

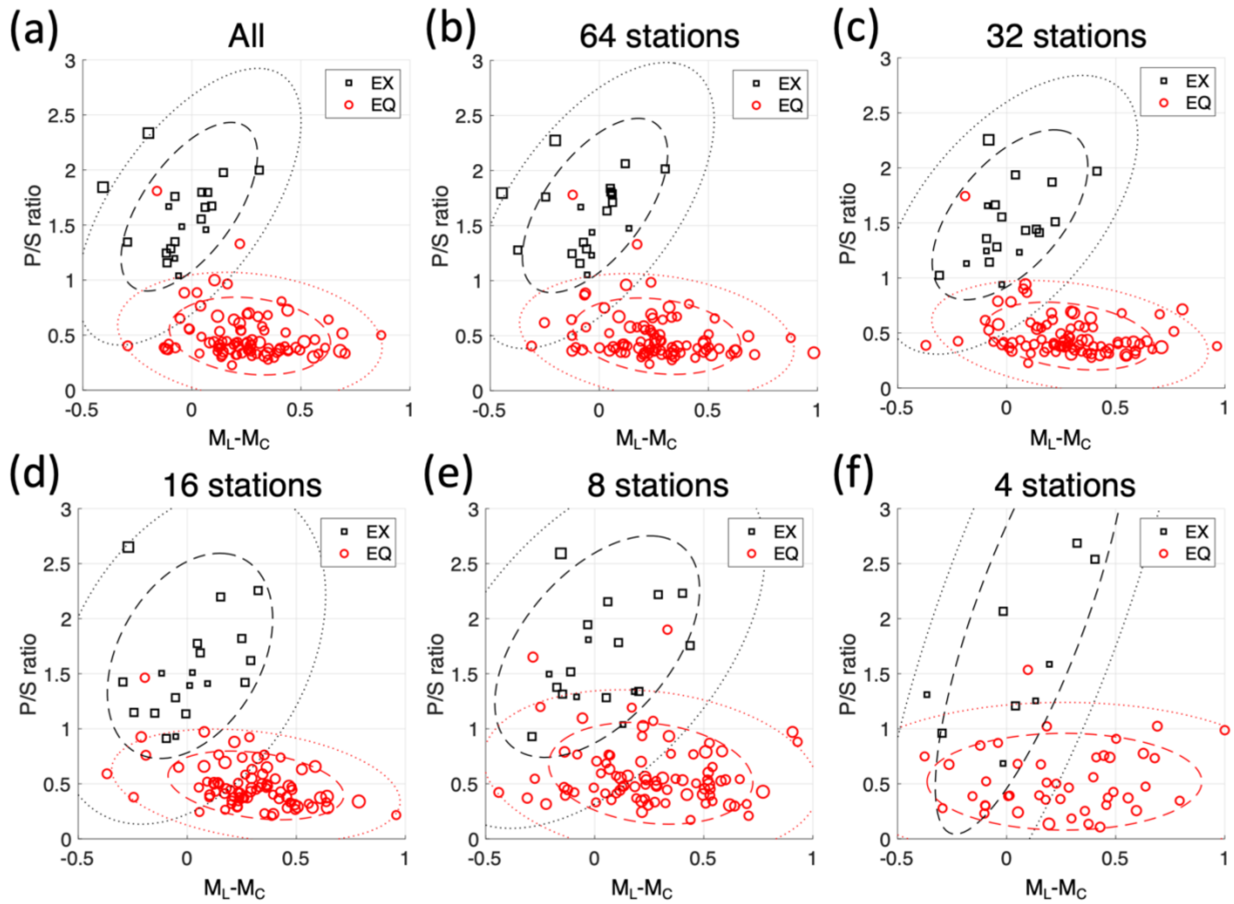

Figure S7. Discrimination performance in the joint domain with decreased stations. The MSH dataset is used for this example (i.e., corresponding to Figure 3a in the main text). In all figures, the dashed and dotted ellipses are the covariance of one and two standard deviations, respectively. Note the overlapped region between the EQ and EX ellipses increases with decreased station number, which will be quantified as lower Mahalanobis distances.

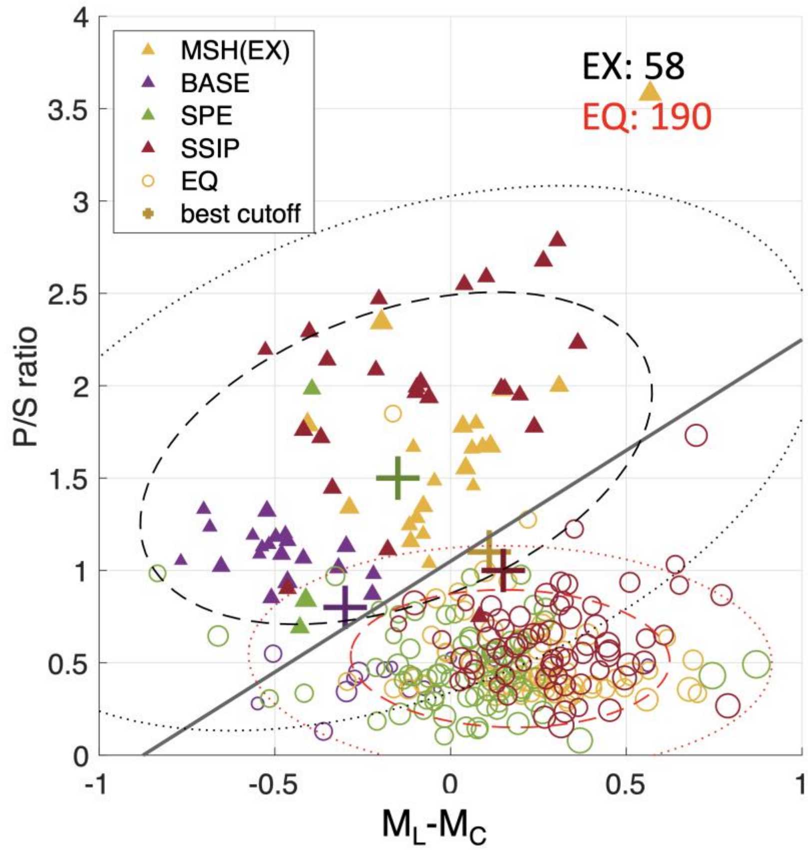

Figure S8. Discrimination results in the joint coordinate using stations within 100 km (i.e., same as Figure 4a in the main text but limiting to 100 km). (a) All event-based P/S or M_L-M_C of the four datasets as labeled. The cross symbols mark the best P/S and M_L-M_C cut offs for each dataset, determined from the ROC and AUC curves (see Figure 2). The dashed and dotted ellipses are the covariance of one and two standard deviations, respectively. The grey line marks the best joint discrimination threshold.

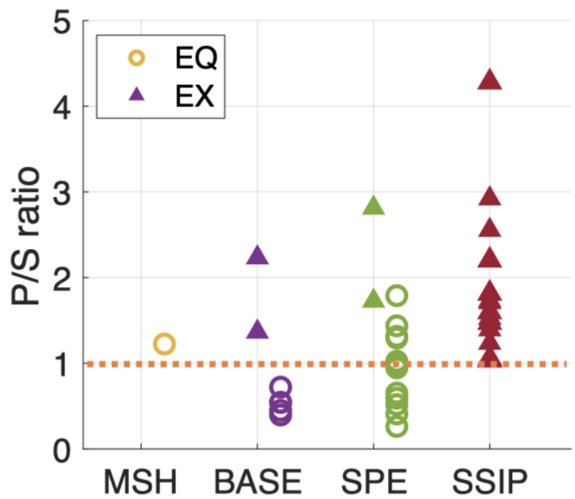

Figure S9. P/S ratio for the 23 earthquakes and 21 explosive events that are not analyzed in the joint domain due to low (<3) or missing valid stations. Five earthquakes from SPE are missing P/S measurements, thus, are not shown. The orange dotted line marks an optimal P/S cutoff of 1.

Table S1. Explosives reported as earthquakes by USGS from SSIP. The reported origin times of the six events are within 0.2–2.4 sec of and co-located with the six shots on March 6, 2011.

Catalog Time (UTC)	**Catalog Latitude**	**Catalog Longitude**	**Catalog Depth**	**Catalog M_L**	***Shot ID***	***True time (UTC)***	***True Latitude***	***True Longitude***	***Load (kg)***
2011-03-06 12:09:02.400	32.703	-115.260	10	2	*10460*	*12:09*	*32.69438*	*-115.25193*	1367
2011-03-06 10:33:00.400	32.677	-116.386	3	1.8	*20550*	*10:33*	*32.67207*	*-116.34656*	*911*
2011-03-06 10:12:01.620	32.841	-115.367	13	1.7	*10670*	*12:12*	*32.84924*	*-115.3718*	458
2011-03-06 10:09:01.370	32.981	-115.205	4.8	1.7	*21640*	*10:09*	*32.9638338*	*-115.2313188*	*592*
2011-03-06 09:02:59.800	32.59	-116.693	0.6	1.5	*20220*	*09:03*	*32.6008*	*-116.68154*	*684*
2011-03-06 07:15:01.490	32.879	-115.535	17.2	2.1	*21330*	*07:15*	*32.8851499*	*-115.5409971*	*911*

Table S2. [uploaded separately] Datasets showing all the events and explosives used for the four regions, with event-based P/S, M_L, and M_C calculated (as well as the number of stations used for each measurement). For the "Source Type" in the last column of each sheet: 0-explosive, 1-earthquake, 4-mine blast.